Engineering Fracture Mechanics 272 (2022) 108721

Contents lists available at ScienceDirect

Engineering Fracture Mechanics

journal homepage: www.elsevier.com/locate/engfracmech

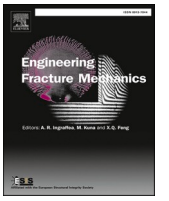

Mechanism of artificial surface defect induced cracking for very high cycle fatigue of Ti alloys

Jian Sun [a,b], Wenjie Peng [c], Chengqi Sun [a,b,*]

[a] State Key Laboratory of Nonlinear Mechanics, Institute of Mechanics, Chinese Academy of Sciences, Beijing 100190, China
[b] School of Engineering Science, University of Chinese Academy of Sciences, Beijing 100049, China
[c] Baosteel Central Research Institute, Wuhan 430080, China

ARTICLE INFO

Keywords:
TC17 titanium alloy
Artificial surface defect
Very high cycle fatigue
Crack initiation mechanism
Deformation twins

ABSTRACT

In-situ observation of crack growth and electron backscatter diffraction observation of microstructure around artificial surface defect and at mated crack surfaces are conducted for very high cycle fatigue (VHCF) of TC17 alloy. The artificial surface defect induced VHCF failure presents no slow process of crack initiation and early growth accompanied with nanograin formation commonly observed for internal cracking induced VHCF. It is attributed to the synergistic effect of cyclic stress with time dependent process (e.g. the influence of moisture, action of hydrogen, etc.). The nanograins and deformation twins are also observed in some α grains at or near crack surfaces.

1. Introduction

In recent decades, numerous studies have shown that the metallic materials could still fail at the fatigue cycles exceeding 10^7 (i.e. very high cycle fatigue, VHCF) [1–7]. Scanning electron microscope (SEM) observation indicates that the crack initiation and early growth region often exhibits fine granular area (FGA) or rough area (RA) characteristic for high strength steels and titanium alloys failed in VHCF regime [8–14]. Transmission electron microscope (TEM) and electron backscatter diffraction (EBSD) observations further indicate that the microstructure in FGA or RA changes in some cases, which could be local regions of nanograins or a layer of nanograins [11,13–18]. Some models have also been proposed for the formation of FGA or RA [15,19–23]. For example, one view is that FGA or RA formation is due to the dislocation interaction caused by the locally high strain [10,14,17,24–26].

Recently, the intermediate process of internal crack initiation and early growth in VHCF regime was successfully captured for high strength steels and titanium alloys by using the two-step variable amplitude loadings [14,25,27]. Based on the "tree ring" like marks left on the fatigue fracture surface, the equivalent crack growth rate in crack initiation and early growth stage is lower than 10^{-10} m/cyc and the equivalent crack growth rate increases with increasing the loading cycle. The captured secondary crack initiation and early growth region with FGA feature further validates this evolutionary process of the internal crack initiation and early growth [27,28].

Defect is an important factor affecting the fatigue behavior, which could significantly reduce the fatigue strength or fatigue life of metallic materials [29–31]. Usually, defects are inevitable in the process of component manufacturing and service. Therefore, it is of great significance to investigate the effect of defect on VHCF behavior of metallic materials. Existing studies have shown that the crack

* Corresponding author at: State Key Laboratory of Nonlinear Mechanics, Institute of Mechanics, Chinese Academy of Sciences, Beijing 100190, China.
E-mail address: scq@lnm.imech.ac.cn (C. Sun).

https://doi.org/10.1016/j.engfracmech.2022.108721
Received 6 July 2022; Received in revised form 30 July 2022; Accepted 7 August 2022
Available online 10 August 2022

initiation and early growth region often presents FGA or RA characteristic for the internal defect induced VHCF failure, and the *S*—*N* data exhibit continuous descending feature in high cycle and VHCF regimes [8,9,27,28,32]. The nanograin formation is also commonly observed in FGA for the internal defect induced VHCF failure [10,12,14,15,17,33]. However, for the artificial surface defect induced failure, the *S*—*N* data tend to have plateau region feature in VHCF regime or in high cycle fatigue regime with longer fatigue life and VHCF regime for titanium alloys [18,28,34] and high strength steels [30,33,35,36]. Moreover, unlike the internal defect induced VHCF failure, no FGA feature and nanograin formation for the microstructure were observed on the fracture surface around the defect for the TC17 titanium alloy [18] and the structural steel in VHCF regime [33]. This indicates that the process of artificial surface defect induced VHCF failure should be different from that of the commonly observed VHCF failure from internal crack initiation. However, the previous studies mainly focus on the mechanism of internal cracking induced VHCF failure and the artificial surface defect induced VHCF mechanism still remains unclear. What is the mechanism of the artificial surface defect induced VHCF failure? How is the crack initiation and evolution? These need to be further investigated and elucidated.

In this paper, we aim to explore the mechanism of artificial surface defect induced cracking for VHCF of titanium alloys. At first, fatigue tests are conducted on a TC17 titanium alloy used for compressor blades in aero-engines by an ultrasonic frequency fatigue testing system. The in-situ observation is used to capture the crack growth of specimens during VHCF test. The microstructures around artificial surface defects and at mated crack surfaces after VHCF loading are observed by SEM and EBSD. Finally, the mechanism of artificial surface defect induced cracking in VHCF regime is analyzed and discussed based on the experimental results. The paper indicates that the artificial surface defect induced cracking in VHCF regime is not a purely cyclic loading dominated process, which is due to the synergistic effect of cyclic stress with time dependent process (e.g. the influence of moisture, action of hydrogen, etc.) during the long terms of cyclic loadings.

2. Materials and methods

2.1. Materials and microstructures

The material used in this paper is a TC17 titanium alloy. The chemical composition is 4.97 Al, 4.19 Cr, 4.12 Mo, 2.09 Sn, 1.90 Zr, 0.11O, <0.10 Fe and balanced Ti in weight percent. The material was firstly under beta forging, then solid solution for 4 h at 800 °C and cooled by water, and finally under aging treatment for 8 h at 620 °C. All the specimens were cut from the solid bar after heat treatment. The yield strength is 1061 MPa and the tensile strength is 1145 MPa. The microstructure is basketweave with lamellar α phase. The microstructure parallel to the loading direction is shown in Fig. 1.

2.2. Testing methods

The plate specimen with artificial surface defect is used in this study. The defect is fabricated by a small drill, which is located in the middle of the gauge section with 8 mm width face of the smooth specimen shown in Fig. 2a. The gauge section of the smooth specimen is ground and polished before the defect is drilled. The shape of the defect is shown in Fig. 2b, which refers to the SEM images of the fatigue fracture surface of some failed specimens. The average width *w* of the defect is 332 μm, and the average depth *h* is 157 μm. The fatigue test was conducted on an ultrasonic fatigue testing machine USF-2000A ($f = 20$ kHz). The cyclic stress is controlled by the output displacement of the device, and the applied stress at the gauge section is at first transformed to the displacement by the theoretical formula [37,38]. The stress ratio *R* was –1, and the fatigue loading without intermittence was used. During the fatigue test, the compressive cold air was used to reduce the temperature of the specimen.

The fatigue fracture surfaces were observed by SEM. Moreover, one sample was cut from a failed specimen in VHCF regime and

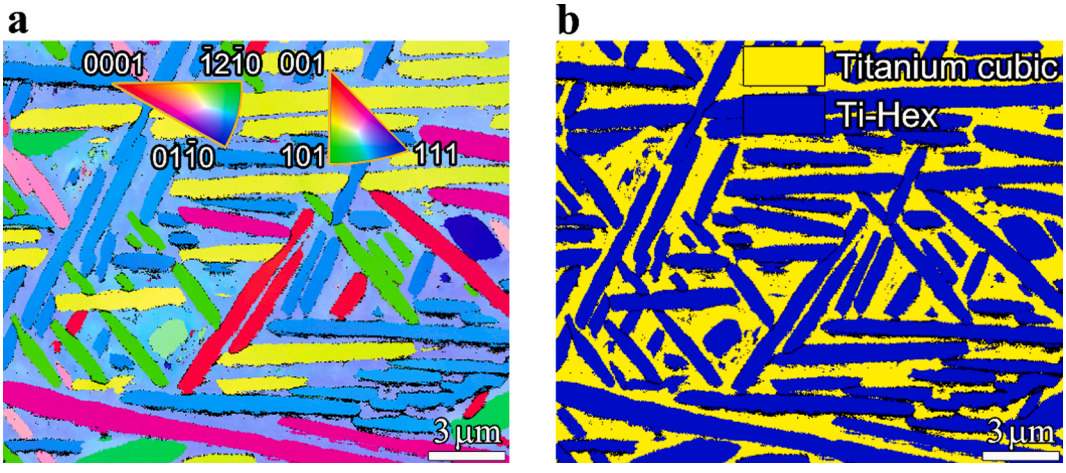

Fig. 1. EBSD observation of microstructure. a: Inverse pole figure (IPF); b: Phase map.

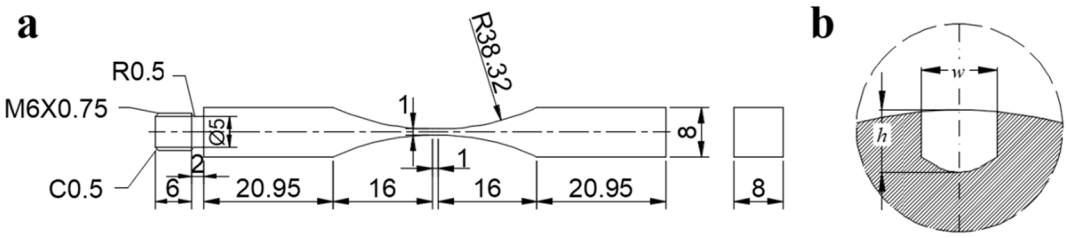

Fig. 2. Shape and geometry of the fatigue specimen (in mm). a: Smooth specimen; b: Sketch map of drilled defect.

another one was cut from an unbroken specimen experiencing VHCF loading. They were both polished parallel to the loading direction, and then observed by SEM and EBSD to further reveal the microstructure characteristic around the artificial surface defect, along the crack surfaces and at crack tips. The in-situ observation by a microscope was also used to monitor the crack initiation and growth induced by the artificial surface defect in VHCF regime.

3. Experimental results and analyses

3.1. Fatigue performances

Fig. 3 shows the *S*—*N* data of the plate specimen with artificial surface defect, in which the stress amplitude is taken as that of the associated smooth specimen at the gauge section. It is seen that the plate specimen with artificial surface defect fails in high cycle fatigue regime for the relative higher stress amplitude and it could fail in VHCF regime at the relative lower stress amplitude. The *S*—*N* data in VHCF regime presents a plateau region feature, i.e. the stress amplitude does not show the downward trend with increasing the fatigue life in VHCF regime. This phenomenon is also observed in specimens with artificial surface defect of the same TC17 alloy under rotating bending and axial loading fatigue tests [18,34], steels [30,33,35,36] and the additively manufactured Ti-6Al-4 V alloy [28] in VHCF regime or in high cycle fatigue regime with longer fatigue life and VHCF regime. It is different from the internal defect induced fatigue failure that the fatigue strength decreases with increasing the fatigue life in high cycle and VHCF regimes [8,9,27,28,32]. This implies that there is a "critical stress" below which the specimen with artificial surface defect does not fail in VHCF regime.

It is noted that the quality of the drilled defect (e.g. the difference of width *w* and depth *h* of the defect) might have some influence on the fatigue performance. According to the results in literature [18,28,29], the defect size could be an effective parameter for evaluating the influence of defect on the fatigue performance. Here, the defect size is measured for the failed specimens except for the specimens prepared for EBSD observation, and it is between 197 μm and 217 μm. The defect size is taken as the square root of the projection area of the defect on the fatigue fracture surface. Considering that the defect is of small difference in size and it is drilled by the same process, the difference of the drilled defect is negligible in the present paper.

3.2. Fatigue fracture surface morphologies

The fatigue cracks all initiate from the artificial surface defect for the failed specimens. At relative higher stress amplitude, the specimen fails in high cycle fatigue regime. While at relative lower stress amplitude, it fails in VHCF regime. Fig. 4a and b show the fracture surface morphology of the failed specimen in high cycle fatigue regime, and Fig. 4c and d show the fracture surface

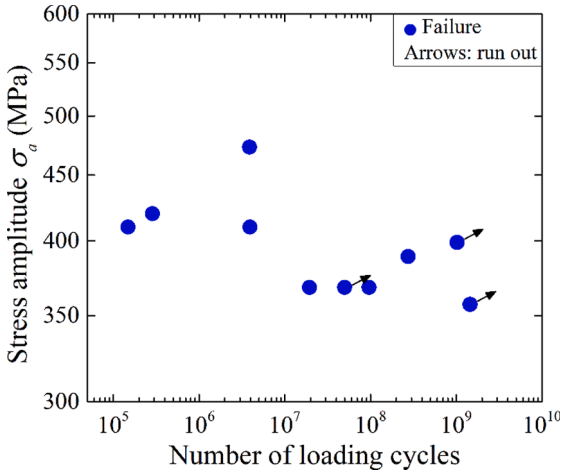

Fig. 3. *S*—*N* data of tested specimens with artificial surface defect.

morphology of the failed specimen in VHCF regime. SEM observation indicates that no FGA or RA feature presents around the defect for all the failed specimens. For the same TC17 alloy, the RA feature is observed for the internal crack initiation of the smooth specimen in high cycle fatigue and VHCF regimes [18,34]. This implies that the failure mechanism of the specimens with artificial surface defect in VHCF regime is different from that of the smooth specimen with RA feature in the crack initiation and early growth region.

3.3. Microstructure observation of mated crack surfaces

In order to understand the process of crack initiation and growth induced by the artificial surface defect in VHCF regime, the microstructures around the defect and at mated crack surfaces of a failed specimen at the stress amplitude $\sigma_a = 368$ MPa and $N_f = 9.61 \times 10^7$ cycles were characterized by SEM and EBSD on the sample parallel to the loading direction. The sample was at first cut from the failed specimen and then a little polished. Fig. 5(a1) shows the picture of a part of the failed specimen, and Fig. 5(a2-a4) shows the SEM images of the mated cracks. It is seen from Fig. 5(a2 and a4) that the crack bifurcates with the crack growth. Fig. 5(b1-b4) shows the SEM image, IPF, phase map and KAM map of the mated cracks (i.e. region B) near the defect in Fig. 5(a3), respectively. Fig. 5(c1-c4) shows the results of the mated cracks (i.e. region C) a little far from the defect in Fig. 5(a3). Fig. 5(d1-d4, e1-e4 and f1-f4) shows the results at a big crack tip (i.e. region D), a bifurcated small crack tip (i.e. region E) and an individual small crack tip (i.e. region F) in Fig. 5(a4), respectively. It is seen from Fig. 5(b2) that there are a few small grains formed in the α grains near the defect at the fracture surface. The small grains are also observed in some α grains a little far (about 60 μm) and far from the defect at or close to the crack surface, as shown in Fig. 5(c2-f2). Moreover, the small grains are found in α grains at the bifurcated small crack tip in Fig. 5(e2) and the individual small crack tip in Fig. 5(f2). This implies that the formation of small grains (some of which are in nano size) in α grains at or close to the crack surface is related to the local high stress at the crack tip during crack growth. The KAM values in Fig. 5(b4-f4) indicates that the grains at crack tips or crack surfaces generally experience larger plastic deformation for the artificial surface defect induced VHCF failure.

4. Discussion

4.1. Twinning and nanograins at or near crack surfaces

Here, the α grains at or near the crack surfaces are carefully examined and twinning is found in some α grains (Fig. 6a–e). The deformation twins are all extension ones, namely that the twinning plane is $\{10\bar{1}2\}$. The twins are determined by the grain boundaries that satisfy the twin mode [39]. These special boundaries are examined by the EBSD data and HKL Channel 5 software in the Oxford Instruments system with a tolerance of ± 5° deviation [40,41]. Twinning is not observed in the α grains for the original material

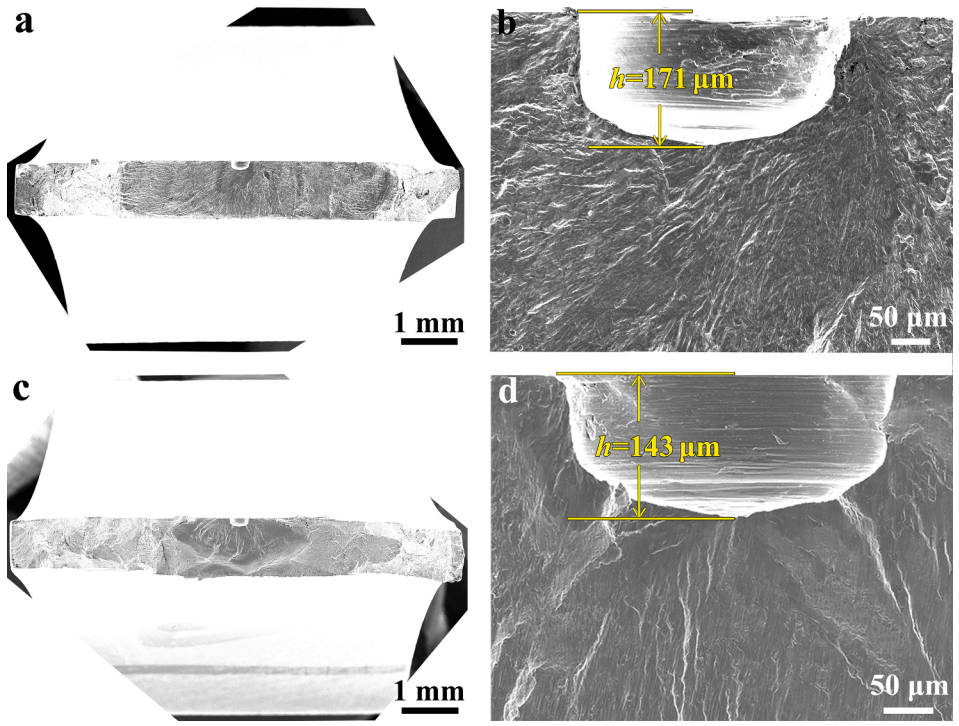

Fig. 4. Fatigue fracture surface morphologies of specimens with artificial surface defect. a and b: $\sigma_a = 420$ MPa, $N_f = 2.86 \times 10^5$ cycles; c and d: $\sigma_a = 368$ MPa, $N_f = 1.95 \times 10^7$ cycles.

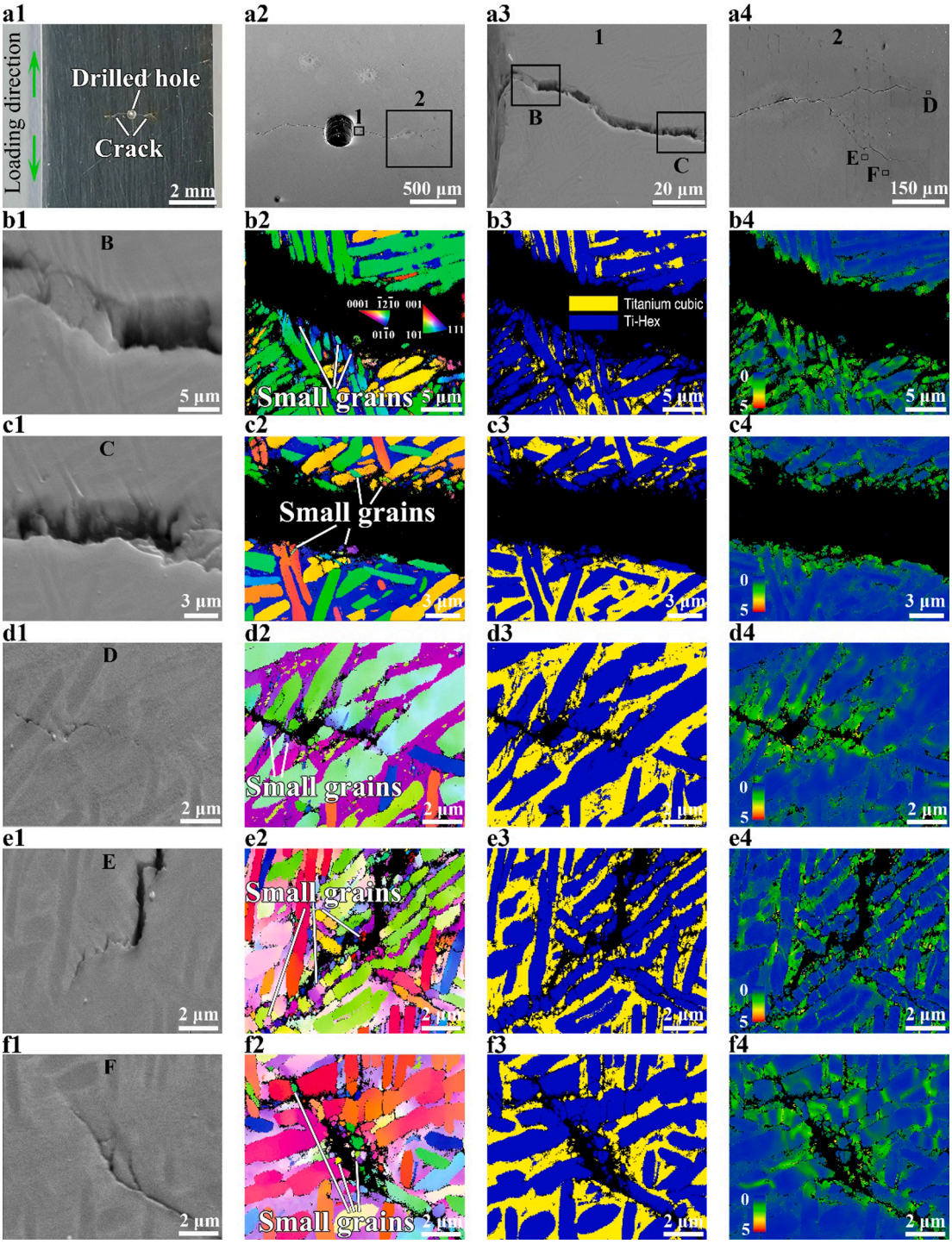

Fig. 5. Observation of mated cracks initiated from artificial surface defect at $\sigma_a = 368$ MPa and $N_f = 9.61 \times 10^7$ cycles. a1: Picture of a part of the failed specimen; a2: SEM image of the mated cracks; a3 and a4: Close-ups of the regions 1 and 2 in a2, respectively; b1-b4 and c1-c4: SEM image, IPF, phase map and KAM map of the rectangular regions B and C in a3, respectively; d1-d4, e1-e4, f1-f4: SEM image, IPF, phase map and KAM map of the rectangular regions D, E and F in a4, respectively.

without experiencing fatigue loading (Fig. 6f), indicating that the deformation twins appear during the fatigue loading. The deformation twins are also observed for the fully lamellar Ti-6Al-4V composed of coarse prior β grains and α lamellas [42] and the Ti-6Al-4V alloy with Widmanstatten microstructure [43]. It was shown that the deformation twins were about 150 μm from the crack surface,

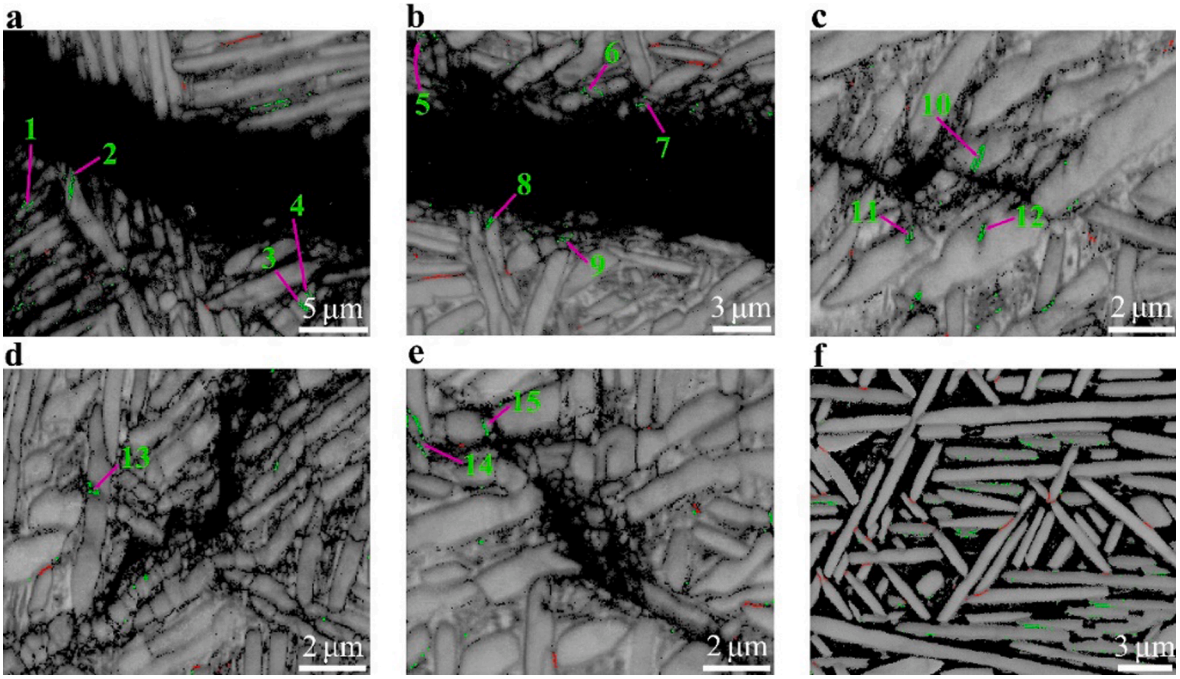

Fig. 6. Deformation twins in α grains. a-e: Deformation twins near the crack surface or at crack tip in Fig. 5(b2-f2), respectively, in which some twin variants are numbered by 1, 2, …, 15; f: Results for the original material in Fig. 1a. Green lines within α grains denote extension twins.

and the thickness, length and density of the deformation twins increased along the crack propagation direction [42]. However, the dependence of deformation twins with crack size is not observed for the present TC17 alloy under VHCF loading. Additionally, Fig. 6 indicates that the deformation twins not only occur from α grain boundaries (e.g. twin variants 10 and 11 in Fig. 6c) but also occur within α grains (e.g. twin variant 12 in Fig. 6c).

Fig. 7 shows the Schmid factors for basal slip and prismatic slip of the parent α grains and the numbered twin variants in Fig. 6a–e. The associated values of the Schmid factors are listed in Table 1. It is seen that some of the $\{10\bar{1}2\}$ twins occur in the parent grain with a bigger Schmid factor for basal slip and the others occur in the parent grain with a smaller Schmid factor for basal slip. When the Schmid factor for prismatic slip is considered, the $\{10\bar{1}2\}$ twins occur in the parent grain with the Schmid factor no less than 0.36 for basal slip or prismatic slip. This indicates that twinning tends to occur in the α grain with bigger Schmid factor for basal slip or prismatic slip. The twin variants have bigger Schmid factor for basal slip or prismatic slip. For the fifteen variants in Fig. 7, the maximum values of the Schmid factors for basal slip and prismatic slip are all no less than 0.38 except one variant with a maximum value of 0.28 for the Schmid factors of basal slip and prismatic slip. Further, Fig. 5(b4-f4) indicates that the KAM values are commonly bigger in the local region where the twins form. This implies that twinning is triggered in the locally high strain region in order to meet the strain

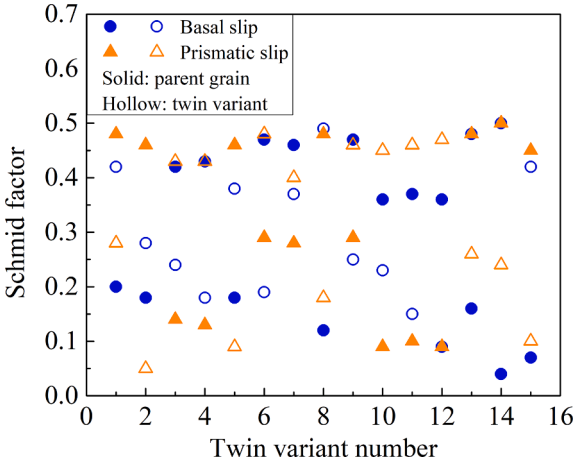

Fig. 7. Schmid factors for basal slip and prismatic slip of parent α grains and numbered twin variants in Fig. 6a-6e.

Table 1
Schmid factors for basal slip and prismatic slip of parent α grains and numbered twin variants in Fig. 6a–e.

No.	Parent grain		Twin variant	
	Basal slip	Prismatic slip	Basal slip	Prismatic slip
1	0.20	0.48	0.42	0.28
2	0.18	0.46	0.28	0.05
3	0.42	0.14	0.24	0.43
4	0.43	0.13	0.18	0.43
5	0.18	0.46	0.38	0.09
6	0.47	0.29	0.19	0.48
7	0.46	0.28	0.37	0.40
8	0.12	0.48	0.49	0.18
9	0.47	0.29	0.25	0.46
10	0.36	0.09	0.23	0.45
11	0.37	0.10	0.15	0.46
12	0.36	0.09	0.09	0.47
13	0.16	0.48	0.48	0.26
14	0.04	0.50	0.50	0.24
15	0.07	0.45	0.42	0.10

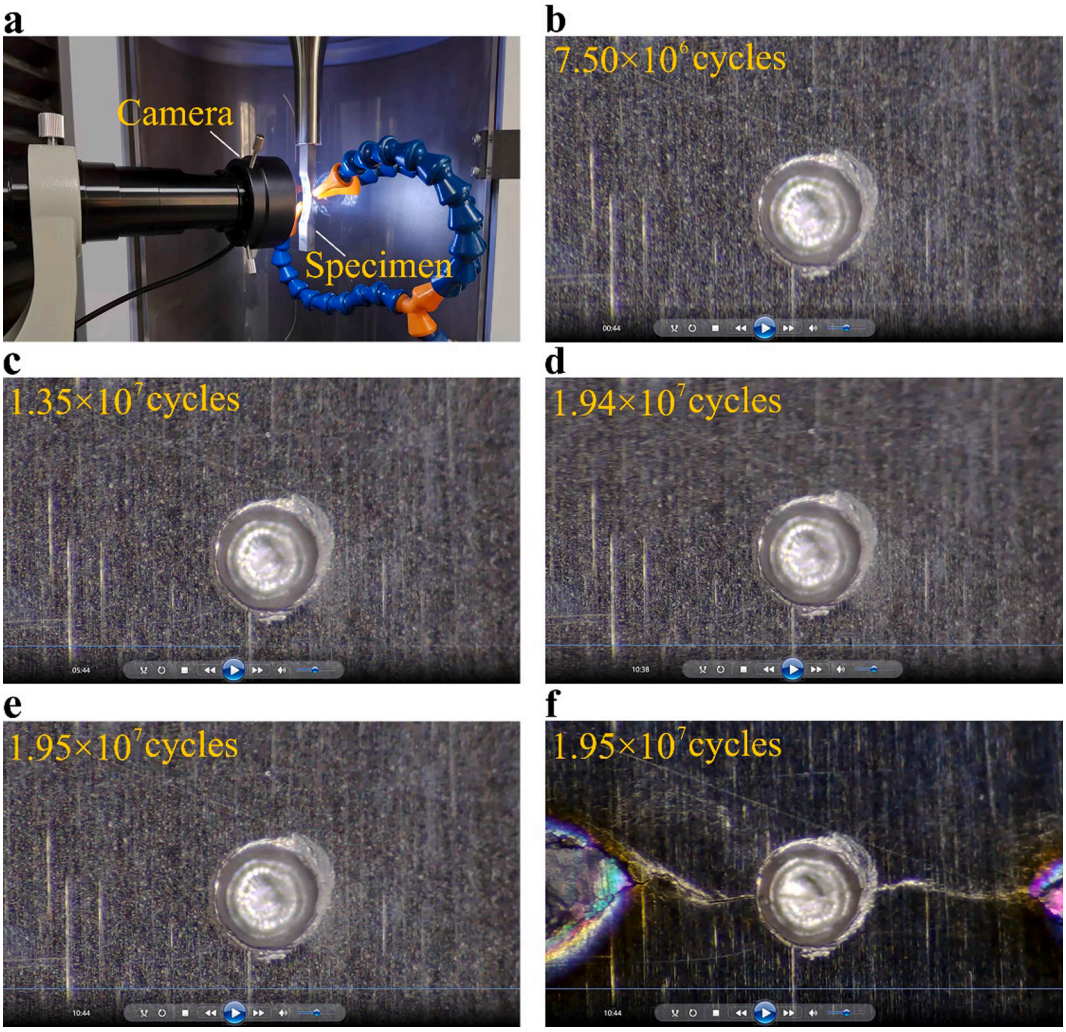

Fig. 8. Picture of in-situ observation of the specimen failed at $\sigma_a = 368$ MPa and $N_f = 1.95 \times 10^7$ cycles. Loading direction is up and down along the paper.

compatibility requirement. It is noted that the Schmid factor for basal slip or prismatic slip could have some difference at different positions for a given α grain due to the deformation inhomogeneity. In this case, the maximum value of the Schmid factors for basal slip at different positions and the maximum value of the Schmid factor for prismatic slip at different positions are used in Fig. 7.

Twinning often occurs in hexagonal close-packed metals and alloys due to the lack of slip systems for dislocation glide. It could contribute to the plastic deformation and release the stress intensification at crack tip [42,43]. The results in Figs. 5 and 6 indicate that the deformation twins play an important role in the nanograin formation in α grains. In fact, some of twin variants (e.g. twin variants 8 and 9 in Fig. 6b) are nanoscale grains. The local high stress concentration at crack tip induces twinning or slip in preferentially oriented α grains [42,44]. Then, the interaction between twin systems or dislocations causes the formation of dislocation cells or walls, the nucleation of microbands, and finally the nanograins [45–47].

4.2. *Artificial surface defect induced cracking mechanism*

4.2.1. *In-situ observation of crack growth*

In order to further understanding the artificial surface defect induced crack initiation and evolution process in VHCF regime, the in-situ observation was carried out for the specimen under the stress amplitude $\sigma_a = 368$ MPa by a microscope shown in Fig. 8a. The maximum resolution of the microscope is up to 3 μm. It is found that the time is very short (within 1 s) from the crack occurrence to a very large crack on the specimen surface, as shown in Fig. 8b–f. Considering that the loading frequency is 20 kHz for the fatigue test, it is less than 20, 000 cycles from the crack occurrence to a very large crack on the specimen surface, namely that the crack growth process consumes a very small part of the total fatigue life for the artificial surface defect induced VHCF failure of the present TC17 alloy.

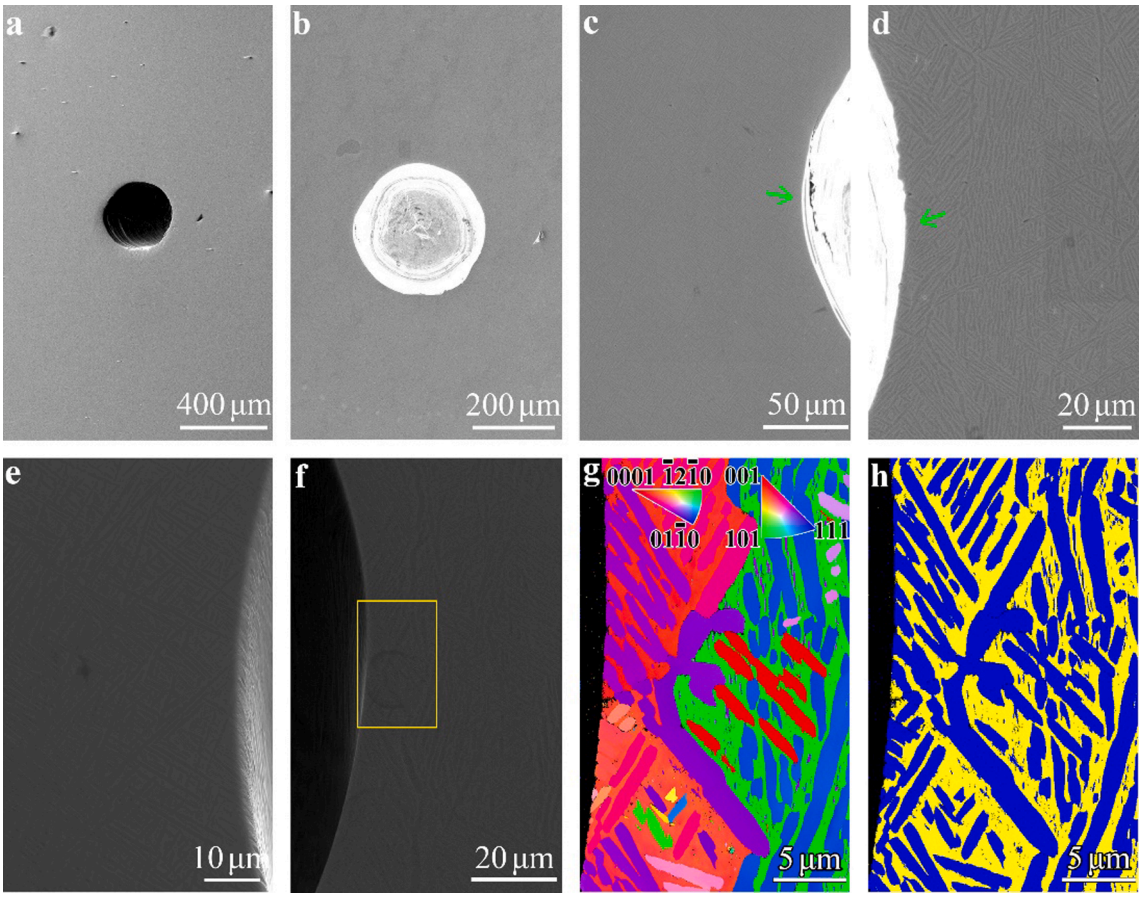

Fig. 9. SEM and EBSD observations of microstructure around artificial surface defect after 5×10^7 cycles under the stress amplitude $\sigma_a = 368$ MPa. a: Observed surface about 10 μm depth from the specimen surface; b: Observed surface about 50 μm from the specimen surface; c and d: Parts of the observed surface about 100 μm from the specimen surface; e and f: Close-ups of the local regions where the arrows point in c and d, respectively; g and h: IPF and phase map of the rectangular region in f, respectively, the blue and yellow colors in h denote α phase and β phase, respectively. Loading direction is up and down along the paper.

4.2.2. Microstructures around defect after VHCF loading

SEM observation in Fig. 4c and d indicates that the fracture surface around the artificial surface defect exhibits no FGA or RA feature as that commonly observed for the internal crack initiation induced VHCF failure. In Fig. 5, just a few small grains are found in some α grains near and a little far from the defect at the fracture surface for the artificial surface defect induced VHCF failure. It is consistent with the results that no grain refinement phenomenon is observed in a very small region (about 5 μm) at and near the crack surface for the same TC17 alloy [18] and a structural steel [33] failed from the artificial surface defect in VHCF regime.

For a further examination of the microstructure characteristic and damage evolution around the artificial surface defect during VHCF loading, postmortem observations were conducted on the sample cut from the gauge section of a specimen experiencing 5×10^7 cycles under the stress amplitude $\sigma_a = 368$ MPa. Three polished surfaces of the sample are observed, and they are all parallel to the loading direction. One observed surface is just a little polished, which is about 10 μm depth from the specimen surface. The other two are about 50 μm and 100 μm depths from the specimen surface, respectively. The depth is determined by the measurement of the sample's thickness. The SEM and EBSD results of the observed surfaces are shown in Fig. 9. No micro cracks appear at or in the vicinity of the artificial surface defect from the SEM observation in Fig. 9a–f. The grain refinement phenomenon is also not observed for the microstructure near the artificial surface defect, as shown in Fig. 9g and h. The results in Figs. 5 and 9 indicate that the majority of the fatigue life consumed in VHCF is irrespective of the microstructure change (e.g. grain refinement) or small crack formation. This differs from that of the internal cracking induced VHCF failure, in which the nanograin formation are commonly observed in the crack initiation and early growth region [10,12,14,15,17,33] and the crack grows very slowly in the crack initiation and early growth stage [14,25,27].

The results in Figs. 4, 5, 8 and 9 indicate that this kind of VHCF behavior, such as the VHCF of the present TC17 alloy with artificial surface defect and the VHCF of a structural steel with artificial surface defect [33], is not a purely cyclic loading dominated process. In this case, the crack initiation is due to the synergistic effect of cyclic stress and time dependent process (e.g. the influence of moisture, action of hydrogen, etc.) during the long terms of cyclic loadings. For example, a weak corrosive atmosphere could cause the surface pitting during the cyclic loading and a combined action of the surrounding medium and the cyclic stress promotes the formation of a micro or small fatigue crack that the cyclic stress alone can cause the fatigue crack to continue to grow [48,49]. In other words, the specimen does not fail under the stress (e.g. in the plateau region) alone if there is no other factors. The factors such as corrosion and action of hydrogen or the synergistic effect with cyclic stress degenerate the fatigue resistance of the material at artificial surface defect during the cyclic loading and promote the crack initiation. Once the crack initiates, the crack grows fast due to the local high stress caused by the artificial surface defect, and results in the eventual failure. This can explain the reason why some specimens fail at very long fatigue life in the plateau region of the *S*—*N* data. This can also explain the observation that it consumes a small number of cycles from the crack occurrence to a very large crack on the specimen surface. The mechanism of artificial surface defect induced cracking differs from that caused by the internal cracking in VHCF regime. For the latter, the crack initiation and early growth consumes almost the total fatigue life in VHCF regime and it is often accompanied with nanograin formation [7,14,25,27]. The crack nucleation or fatigue damage is dominated by the cyclic loading, and the factors (e.g. environmental medium) have no or negligible influence on the fatigue behavior.

It is noted that, for the specimen tested in air, the influence of surrounding environment (e.g. moisture) or the synergistic effect of cyclic stress and environment is generally very small. Therefore, the *S*—*N* data of specimens with artificial surface defect could present the plateau region feature in VHCF regime. While for the specimen tested in corrosive medium such as water vapor and salt water, the influence of medium on the fatigue property becomes heavier especially with the increase of the testing time. In this case, besides the influence of environment itself, the synergistic effect of cyclic stress and environment might also become significant, and the *S*—*N* data of specimens (with artificial surface defect or notch) could be a downward trend, as shown in literature [50,51]. It is also noted that, due to the difference of the material and defect type, the specimen could initiate non-propagating micro or small cracks at artificial surface defect after a number of cyclic loadings in some cases [29,34,49]. In this case, the *S*—*N* data could also present the plateau region feature in VHCF regime.

5. Conclusions

In this paper, the artificial surface defect induced VHCF behavior is investigated for the TC17 alloy used for compressor blades in aero-engines. The main results are as follows.

(1) EBSD observation of the mated crack surfaces indicates that there are nanograin formation and twinning phenomenon in α grains at crack tip and at or near the crack surface. The nanograins and deformation twins are attributed to the local high stress at crack tip during the crack growth.
(2) Differing from that commonly observed for internal cracking induced VHCF, the artificial surface defect induced VHCF failure does not present the slow process of crack initiation and early growth accompanied with nanograin formation. It is essentially due to the synergistic effect of cyclic stress and time dependent process (e.g. the influence of moisture in surrounding environment, the action of hydrogen, etc.) during the long terms of cyclic loadings. Once the crack initiates, it grows fast and leads to the eventual failure in a small number of loading cycles.
(3) The findings provide a further understanding of the process of fatigue failure induced by artificial surface defect in VHCF regime. It explains the reason why some specimens fail at very long fatigue life in the plateau region of the *S*—*N* data and why the SEM images present the crack propagation feature near artificial surface defect in VHCF regime. The paper also indicates

that it is hard to evaluate the fatigue life of materials or structures through the crack growth behavior for this kind of VHCF failure.

CRediT authorship contribution statement

Jian Sun: Visualization, Methodology, Investigation, Formal analysis, Writing - original draft, Writing - review & editing. **Wenjie Peng:** Methodology, Investigation, Formal analysis, Writing - review & editing. **Chengqi Sun:** Visualization, Supervision, Methodology, Investigation, Funding acquisition, Formal analysis, Conceptualization, Writing - original draft, Writing - review & editing.

Declaration of Competing Interest

The authors declare that they have no known competing financial interests or personal relationships that could have appeared to influence the work reported in this paper.

Data availability

Data will be made available on request.

Acknowledgements

The authors gratefully acknowledge the support from the National Natural Science Foundation of China Basic Science Center for "Multiscale Problems in Nonlinear Mechanics" (11988102) and the National Natural Science Foundation of China (91860112).

References

[1] Zhao Z, Liang Z, Li Q, Zhang F, Chen B. Crack initiation and propagation behaviour under high-temperature Very-High-Cycle fatigue: Directionally solidified columnar-grained vs. single-crystal superalloys. Mater Sci Eng A 2022;836:142711.
[2] Gao G, Liu R, Fan Y, Qian G, Gui X, Misra RDK, et al. Mechanism of subsurface microstructural fatigue crack initiation during high and very-high cycle fatigue of advanced bainitic steels. J Mater Sci Technol 2022;108:142–57.
[3] Xu W, Zhao Y, Chen X, Zhong B, Yu H, He Y, et al. An ultra-high frequency vibration-based fatigue test and its comparative study of a titanium alloy in the VHCF regime. Metals 2020;10:1415.
[4] Li Y, Song Q, Feng S, Sun C. Effects of loading frequency and specimen geometry on high cycle and very high cycle fatigue life of a high strength titanium alloy. Materials 2018;11:1628.
[5] Spriestersbach D, Brodyanski A, Lösch J, Kopnarski M, Kerscher E. Very high cycle fatigue of bearing steels with artificial defects in vacuum. Mater Sci Technol 2016;32(11):1111–8.
[6] Huang Z, Liu H, Wang H, Wagner D, Khan M, Wang Q. Effect of stress ratio on VHCF behavior for a compressor blade titanium alloy. Int J Fatigue 2016;93:232–7.
[7] Hong Y, Sun C. The nature and the mechanism of crack initiation and early growth for Very-High-Cycle fatigue of metallic materials-An overview. Theor Appl Fract Mech 2017;92:331–50.
[8] Shiozawa K, Hasegawa T, Kashiwagi Y, Lu L. Very high cycle fatigue properties of bearing steel under axial loading condition. Int J Fatigue 2009;31(5):880–8.
[9] Nakajima M, Tokaji K, Itoga H, Shimizu T. Effect of loading condition on very high cycle fatigue behavior in a high strength steel. Int J Fatigue 2010;32(2):475–80.
[10] Grad P, Reuscher B, Brodyanski A, Kopnarski M, Kerscher E. Mechanism of fatigue crack initiation and propagation in the very high cycle fatigue regime of high-strength steels. Scr Mater 2012;67(10):838–41.
[11] Su H, Liu X, Sun C, Hong Y. Nanograin layer formation at crack initiation region for Very-High-Cycle fatigue of a Ti-6Al-4V alloy. Fatigue Fract Eng Mater Struct 2017;40(6):979–93.
[12] Hu Y, Sun C, Hong Y. Crack growth rates and microstructure feature of initiation region for Very-High-Cycle fatigue of a high-strength steel. Fatigue Fract Eng Mater Struct 2018;41(8):1717–32.
[13] Sun C, Chi W, Wang W, Duan Y. Characteristic and mechanism of crack initiation and early growth of an additively manufactured Ti-6Al-4V in very high cycle fatigue regime. Int J Mech Sci 2021;205:106591.
[14] Chi W, Li G, Wang W, Sun C. Interior initiation and early growth of very high cycle fatigue crack in an additively manufactured Ti-alloy. Int J Fatigue 2022;160:106862.
[15] Hong Y, Liu X, Lei Z, Sun C. The formation mechanism of characteristic region at crack initiation for Very-High-Cycle fatigue of high-strength steels. Int J Fatigue 2016;89:108–18.
[16] Tofique MW, Bergström J, Svensson K. Very high cycle fatigue of cold rolled stainless steels, crack initiation and formation of the fine granular area. Int J Fatigue 2017;100:238–50.
[17] Sun C, Song Q, Zhou L, Liu J, Wang Y, Wu X, et al. The formation of discontinuous gradient regimes during crack initiation in high strength steels under very high cycle fatigue. Int J Fatigue 2019;124:483–92.
[18] Chi W, Wang W, Xu W, Li G, Chen X, Sun C. Effects of defects on fatigue behavior of TC17 titanium alloy for compressor blades: Crack initiation and modeling of fatigue strength. Eng Fract Mech 2022;259:108136.
[19] Murakami Y, Nomoto T, Ueda T, Murakami Y. On the mechanism of fatigue failure in the superlong life regime (N>107 cycles). Part 1: Influence of hydrogen trapped by inclusions. Fatigue Fract Eng Mater Struct 2000;23:893–902.
[20] Shiozawa K, Morii Y, Nishino S, Lu L. Subsurface crack initiation and propagation mechanism in high-strength steel in a very high cycle fatigue regime. Int J Fatigue 2006;28(11):1521–32.
[21] Ogawa T, Stanzl-Tschegg SE, Schönbauer BM. A fracture mechanics approach to interior fatigue crack growth in the very high cycle regime. Eng Fract Mech 2014;115:241–54.
[22] Sakai T, Oguma N, Morikawa A. Microscopic and nanoscopic observations of metallurgical structures around inclusions at interior crack initiation site for a bearing steel in very high-cycle fatigue. Fatigue Fract Eng Mater Struct 2015;38:1305–14.
[23] Zhu M, Jin L, Xuan F. Fatigue life and mechanistic modeling of interior micro-defect induced cracking in high cycle and very high cycle regimes. Acta Mater 2018;157:259–75.
[24] Wang C, Liu Y, Nikitin A, Wang Q, Zhou M. A general scenario of fish-eye crack initiation on the life of high-strength steels in the very high-cycle fatigue regime. Fatigue Fract Eng Mater Struct 2019;42(9):2183–94.

[25] Song Q, Sun C. Mechanism of crack initiation and early growth of high strength steels in very high cycle fatigue regime. Mater Sci Eng A 2020;771:138648.
[26] Zhang H-J, Yu F, Li S-X, He E-G. Fine granular area formation by damage-induced shear strain localization in Very-High-Cycle fatigue. Fatigue Fract Eng Mater Struct 2021;44(9):2489–502.
[27] Sun C, Song Q, Zhou L, Pan X. Characteristic of interior crack initiation and early growth for high cycle and very high cycle fatigue of a martensitic stainless steel. Mater Sci Eng A 2019;758:112–20.
[28] Chi W, Wang W, Li Y, Xu W, Sun C. Defect induced cracking and modeling of fatigue strength for an additively manufactured Ti-6Al-4V alloy in very high cycle fatigue regime. Theor Appl Fract Mech 2022;119:103380.
[29] Murakami Y. Metal fatigue: Effects of small defects and nonmetallic inclusions. Academic Press; 2019.
[30] Zhang J, Li H, Yang B, Wu B, Zhu S. Fatigue properties and fatigue strength evaluation of railway axle steel: Effect of micro-shot peening and artificial defect. Int J Fatigue 2020;132:105379.
[31] Hu YN, Wu SC, Withers PJ, Zhang J, Bao HYX, Fu YN, et al. The effect of manufacturing defects on the fatigue life of selective laser melted Ti-6Al-4V structures. Mater Des 2020;192:108708.
[32] Murakam Y, Nomoto T, Ueda T. Factors influencing the mechanism of superlong fatigue failure in steels. Fatigue Fract Eng Mater Struct 1999;22(7):581–90.
[33] Jiang Q, Sun C, Liu X, Hong Y. Very-High-Cycle fatigue behavior of a structural steel with and without induced surface defects. Int J Fatigue 2016;93:352–62.
[34] Li G, Sun C. High-temperature failure mechanism and defect sensitivity of TC17 titanium alloy in high cycle fatigue. J Mater Sci Technol 2022;122:128–40.
[35] Akiniwa Y, Miyamoto N, Tsuru H, Tanaka K. Notch effect on fatigue strength reduction of bearing steel in the very high cycle regime. Int J Fatigue 2006;28(11):1555–65.
[36] Schönbauer BM, Ghosh S, Kömi J, Frondelius T, Mayer H. Influence of small defects and nonmetallic inclusions on the high and very high cycle fatigue strength of an ultrahigh-strength steel. Fatigue Fract Eng Mater Struct 2021;44(11):2990–3007.
[37] Bathias C, Paris PC. Gigacycle fatigue in mechanical practice. CRC Press; 2004.
[38] Peng W, Xue H, Ge R, Peng Z. The influential factors on very high cycle fatigue testing results. MATEC Web Conf 2018;165:20002.
[39] Crawforth P. Towards a micromechanistic understanding of imparted subsurface deformation during machining of titanium alloys. University of Sheffield; 2014.
[40] Guan D, Rainforth WM, Ma L, Wynne B, Gao J. Twin recrystallization mechanisms and exceptional contribution to texture evolution during annealing in a magnesium alloy. Acta Mater 2017;126:132–44.
[41] Xu S, Toth LS, Schuman C, Lecomte J-S, Barnett MR. Dislocation mediated variant selection for secondary twinning in compression of pure titanium. Acta Mater 2017;124:59–70.
[42] Zheng X, Zheng S, Wang J, Ma Y, Wang H, Zhou Y, et al. Twinning and sequential kinking in lamellar Ti-6Al-4V alloy. Acta Mater 2019;181:479–90.
[43] Ma Y, Xue Q, Wang H, Huang S, Qiu J, Feng X, et al. Deformation twinning in fatigue crack tip plastic zone of Ti-6Al-4V alloy with Widmanstatten microstructure. Mater Charact 2017;132:338–47.
[44] Jin S, Marthinsen K, Li Y. Formation of 1121 twin boundaries in titanium by kinking mechanism through accumulative dislocation slip. Acta Mater 2016;120:403–14.
[45] Zhu KY, Vassel A, Brisset F, Lu K, Lu J. Nanostructure formation mechanism of α-titanium using SMAT. Acta Mater 2004;52(14):4101–10.
[46] Wen M, Liu G, Gu J-F, Guan W-M, Lu J. Dislocation evolution in titanium during surface severe plastic deformation. Appl Surf Sci 2009;255(12):6097–102.
[47] Wu S, Fan K, Jiang P, Chen S. Grain refinement of pure Ti during plastic deformation. Mater Sci Eng A 2010;527(26):6917–21.
[48] Botvina LR, Petrova IM, Gadolina IV, Levin VP, Demina YA, Soldatenkov AP, et al. High-cycle fatigue failure of low-carbon steel after long-term aging. Inorg Mater 2010;46:1570–7.
[49] Miller KJ, Odonnell WJ. The fatigue limit and its elimination. Fatigue Fract Eng Mater Struct 1999;22(7):545–57.
[50] Beretta S, Carboni M, Fiore G, lo conte A. Corrosion-fatigue of A1N railway axle steel exposed to rainwater. Int J Fatigue 2010;32:952–61.
[51] Qian G, Hong Y, Zhou C. Investigation of high cycle and Very-High-Cycle fatigue behaviors for a structural steel with smooth and notched specimens. Eng Fail Anal 2010;17(7-8):1517–25.